

MATERIALS SCIENCE

Tunable chiral magneto-transport through band structure engineering in magnetic topological insulators $\text{Mn}(\text{Bi}_{1-x}\text{Sb}_x)_2\text{Te}_4$

Peng Chen^{1,2,3†}, Puyang Huang^{1†}, Zeyu Li^{4†}, Jieyi Liu^{5,6}, Qi Yao^{7,8}, Qiang Sun⁹, Ang Li¹⁰, Xinqi Liu^{7,8}, Yifan Zhang¹, Xinyu Cai^{7,8}, Jiuming Liu¹, Liyang Liao¹¹, Guanying Yang¹², Zhongkai Liu^{7,8}, Yumeng Yang¹, Xiaodong Han^{10,13}, Jin Zou^{14,15}, Thorsten Hesjedal^{5,6*}, Zhenhua Qiao^{4,16*}, Xufeng Kou^{1,7*}

Copyright © 2025 The Authors, some rights reserved; exclusive licensee American Association for the Advancement of Science. No claim to original U.S. Government Works. Distributed under a Creative Commons Attribution License 4.0 (CC BY).

Berry curvature and spin texture are representative tuning parameters that govern spin-orbit coupling–related physics and are also the foundation for future device applications. Here, we investigate the impact of the Sb-to-Bi ratio on shaping the electronic band structure and its correlated first- and second-harmonic magneto-transport signals in the intrinsic magnetic topological insulator $\text{Mn}(\text{Bi}_{1-x}\text{Sb}_x)_2\text{Te}_4$. First-principles calculations reveal that the introduction of Sb not only triggers a topological phase transition but also changes the integral of the Berry curvature at the shifted Fermi level, which leads to the reversal of the anomalous Hall resistance polarity for Sb fractions $x > 0.67$. Moreover, it also induces the opposite spin splitting of the valence bands compared to the Sb-free host, and the resulting clockwise/counterclockwise spin chirality gives rise to a tunable unidirectional second-harmonic anomalous Hall response. Our findings pave the way for constructing chiral spin-orbitronic devices through band structure engineering.

INTRODUCTION

Spin-orbit coupling (SOC), characterized by the spin Hall effect (1–4) and the interfacial Rashba effect (5, 6), has exhibited notable potential in various spintronic applications including nonvolatile magneto-resistive random access memory (7, 8), spin logic devices (9, 10), and neuromorphic computing (11, 12). To enable high-performance SOC-based spintronic devices, the key lies in integrating magnetic order and the spin current in an effective manner. For example, in the heavy metal/ferromagnet heterostructures, the spin-orbit torque (SOT) generated from the heavy metal layer can induce spin precession of the magnetic moment in the adjacent ferromagnet layer, thereby fulfilling the magnetization switching function. In this

regard, the spin Hall angle, quantifying the efficiency of charge-to-spin conversion, is found to be 0.13 (Pt) (13), -0.33 (β -W) (14), -0.13 (Ta) (15), and -0.28 (Hf) (16); meanwhile, the critical switching current density is on the order of 10^6 A/cm² at room temperature. Compared to heavy metals, topological insulators were predicted to excel at spin current generation due to the spin-momentum locking mechanism of the topologically nontrivial surface states (17, 18). Experimentally, deterministic SOT-driven magnetization switching has been documented in various topological insulator-based magnetic heterostructures with much higher spin Hall angle values (>1) and lower switching current densities (as low as 10^5 A/cm² at $T = 298$ K and 10^4 A/cm² at cryogenic temperatures) (19–22). As a result, the use of topological insulators for constructing energy-efficient devices has propelled the rapid advancement of spin-orbitronics in the past decade (17, 18).

In general, SOC is closely correlated with the electronic band structure of a given material (5, 23). For example, the intrinsic anomalous Hall response originates from the integration of the Berry curvature of each occupied band across the Fermi sea. It reflects interband coherence, contributing to the anomalous velocity, which is closely tied to the Berry phase in momentum space (24). In the meantime, the direction of the SOC-induced effective magnetic field is determined by the spin chirality at the Fermi surface (E_F) (25, 26). In this context, $\text{Mn}(\text{Bi}_{1-x}\text{Sb}_x)_2\text{Te}_4$ (MBST), which belongs to the family of the intrinsic magnetic topological insulator MnBi_2Te_4 (MBT) (27), is created through the substitution of Bi atoms with Sb atoms in the host MBT matrix (28). In this material system, with increasing the Sb-to-Bi ratio, the modified Berry curvature distribution leads to a topological phase transition (28), and an accompanied Weyl semimetal state may emerge affecting the large negative c -axis longitudinal magnetoresistance (29). Moreover, introducing Sb is also expected to modify the overall spin texture of the energy band. Accordingly, the MBST system may serve as a promising platform for manipulating the SOC-related effects through band structure engineering.

¹School of Information Science and Technology, ShanghaiTech University, Shanghai 201210, China. ²Shanghai Institute of Microsystem and Information Technology, Chinese Academy of Sciences, Shanghai 200050, China. ³University of Chinese Academy of Science, Beijing 101408, China. ⁴International Center for Quantum Design of Functional Materials, CAS Key Laboratory of Strongly-Coupled Quantum Matter Physics, and Department of Physics, University of Science and Technology of China, Anhui 230026, China. ⁵Department of Physics, Clarendon Laboratory, University of Oxford, Oxford OX1 3PU, UK. ⁶Diamond Light Source, Harwell Science and Innovation Campus, Didcot OX11 0DE, UK. ⁷ShanghaiTech Laboratory for Topological Physics, ShanghaiTech University, Shanghai 201210, China. ⁸School of Physical Science and Technology, ShanghaiTech University, Shanghai 201210, China. ⁹State Key Laboratory of Oral Diseases, National Clinical Research Center for Oral Diseases, West China Hospital of Stomatology, Sichuan University, Chengdu, Sichuan 610041, China. ¹⁰Beijing Key Laboratory of Microstructure and Property of Advanced Materials, Beijing University of Technology, Beijing 100124, China. ¹¹Institute for Solid State Physics, University of Tokyo, Kashiwa 277-8581, Japan. ¹²College of Advanced Interdisciplinary Studies and Nanhu Laser Laboratory, National University of Defense Technology, Changsha, Hunan 410073, China. ¹³Department of Materials Science and Engineering, Southern University of Science and Technology, Shenzhen 518055, China. ¹⁴School of Mechanical and Mining Engineering and Centre for Microscopy and Microanalysis, The University of Queensland, QLD 4072, Australia. ¹⁵Institute of Energy Materials Science, University of Shanghai for Science and Technology, Shanghai 200093, China. ¹⁶Hefei National Laboratory, University of Science and Technology of China, Hefei 230088, China.

*Corresponding author. Email: koux@shanghaitech.edu.cn (X.K.); qiao@ustc.edu.cn (Z.Q.); thorsten.hesjedal@physics.ox.ac.uk (T.H.)

†These authors contributed equally to this work.

Here, we report the tuning of the magneto-resistance (MR) and anomalous Hall effect (AHE) responses in five septuple layer (SL) MBST thin films. Both the x -dependent magneto-transport results and the density functional theory (DFT) calculations support our conclusions that the reversal of the first-order AHE polarity stems from the opposite Berry curvatures which are dominant for different Sb concentrations. Moreover, the magnetic field and angular-dependent second-harmonic Hall responses also change the sign for $x > 0.95$, triggered by the switching of spin chirality and potential gradient direction during the MnBi_2Te_4 -to- MnSb_2Te_4 transition. Our findings highlight the importance of Berry curvature and spin texture in tailoring the magneto-transport response. These insights will enable the development of chiral SOT-related device applications based on the magnetic topological insulator MBST.

RESULTS

Structural properties and phase transition calculations of five SL MBST samples

Experimentally, single-crystalline $\text{Mn}(\text{Bi}_{1-x}\text{Sb}_x)_2\text{Te}_4$ thin films were grown on the 2-inch $\text{Al}_2\text{O}_3(0001)$ substrates by molecular beam epitaxy (MBE). Drawing from our prior work, the septuple-layer structure of MBT can be established by alternating the Bi_2Te_3 and MnTe monolayers, followed by a dedicated post-annealing process (30). Following the same basic protocol for the MBST sample growth, we incorporated Sb in the $(\text{Bi}_{1-x}\text{Sb}_x)_2\text{Te}_3$ layer (Fig. 1A). During growth, the structural quality of the films was monitored using in situ reflection high-energy electron diffraction (RHEED). As illustrated in Fig. 1B, the sharp and streaky RHEED patterns of MBT and MnSb_2Te_4 (MST) manifest the two-dimensional epitaxial growth mode. With increasing Sb incorporation, the spacing between the first-order RHEED streaks (which is related to the inverse of the d -spacing of the direct lattice) gradually enlarges from 113 (MBT) to 117.8 (MST) reciprocal lattice units, suggesting that the in-plane lattice constant of MST is reduced by 4.07% compared to that of MBT (31). Consistent with the RHEED data, the Sb concentration x within the MBST samples was also quantified using x -ray photoelectron spectroscopy (fig. S1 and table S1). Moreover, the cross-sectional high-resolution scanning transmission electron microscopy (HR-STEM) images in Fig. 1C and fig. S2 (A and B) visualize the well-ordered SL structures of MBT/MST, while the sharp x -ray diffraction patterns of the MBST samples exhibit a series of $(00n)$ peaks, with no evidence suggesting the presence of a secondary phase (fig. S2, D to F). In addition, the electronic band structure of MBST ($0 \leq x \leq 1$) was investigated by DFT-based first-principles calculations, and the Sb-induced topological phase transition is observed in Fig. 1D. Specifically, a non-trivial topological surface state with a negative E_g , induced by the inverted band, appears in MBT (Fig. 1E) (28). With the increase of the Sb content, the inverted bandgap gradually shrinks (i.e., due to the relatively weakened SOC of the Sb atoms) (28) until it is closed at $x = 0.35$ (i.e., the gapless band structure in Fig. 1F), which indicates the completion of topological phase transition from $C = 1$ to $C = 0$ (where C is the topological Chern number) (28, 32). With further increasing the Sb-to-Bi ratio, the MBST ($x > 0.35$) system maintains the topologically trivial state with a positive energy gap (Fig. 1G) (28, 32). Therefore, our comprehensive materials characterization results and DFT calculations confirm the high quality of the MBE-grown MBST samples and the tunability of the band structure, which makes them perfectly suited for our systematic doping study.

AHE and AHC polarity reversals induced by tunable Berry curvature

Subsequently, a set of five SL MBST-based micrometer-sized six-terminal Hall bar devices was fabricated using standard photolithography and ion beam etching, and their magnetic/electrical properties were investigated by magneto-transport measurements, where the x axis was defined as the current conduction direction and the magnetic field was applied along the z axis (Fig. 2A). As depicted in Fig. 2B, the overall MR responses display two distinctive features. First, the low-field MR curve undergoes a positive-to-negative transition with increasing Sb content (x), which should be associated with the topological phase transition (29). Furthermore, the antiferromagnetic hump-like giant MR profile of the MBT thin film gradually transits into a ferromagnetic-like double-split butterfly MR slope (inset of Fig. 2B) in samples with $x \geq 0.67$. This evolution highlights the role of Sb atoms in modulating the interlayer magnetic coupling within the MBST samples (29). Likewise, the characteristic saturation field (H_s) in reference to the measured anomalous Hall resistance (R_s) monotonically decreases with x (i.e., indicated by the dashed arrow in Fig. 2C), suggesting a weakening trend of interlayer antiferromagnetic coupling. Notably, with further increasing the Sb-to-Bi ratio, the polarity of the AHE hysteresis loop is reversed when $x > 0.67$ (inset of Fig. 2C). Correspondingly, the saturated anomalous Hall resistance (i.e., after subtracting the ordinary Hall component) at $\mu_0 H = 8$ T also changes from negative ($x \leq 0.67$, area I) to positive ($x \geq 0.9$, area II) when $1.6 \text{ K} \leq T \leq 10 \text{ K}$ (Fig. 2D). Here, it should be noted that the charge neutrality points of the MBST samples extracted from the carrier density (n) chart are found to be located at $x \sim 0.14$ in the low-temperature region (Fig. 2E). With the further increase of the Sb content, the Fermi level progressively shifts toward the valence band below the Dirac point, which mainly determines the R_{xy} slope in the high-field region (i.e., yet it does not contribute to the AHE polarity change). Therefore, the systematic MR and R_{xy} results reveal the critical role of the band structure (i.e., by controlling the Sb-to-Bi ratio) in manipulating the magneto-transport behavior and magnetic coupling in the MBST system.

To understand the fundamental origin of the AHE in the five SL-MBST samples, we plotted the normalized anomalous Hall conductance (AHC) $\sigma_{xy}^{\text{AHE}} / \sigma_{xy}^{\text{AHE}}(x=1)$ [where $\sigma_{xy}^{\text{AHE}} = R_{xy} / (R_{xx}^2 + R_{xy}^2)$] as a function of the Sb concentration in Fig. 3A. As can be seen, the signs of the AHC of the $x = 0.45$ and 0.67 samples are opposite to those of the $x = 0.9$ and 1 counterparts. Accompanying this dataset, the intrinsic Hall conductance for different x values was calculated as the integral of the Berry curvature of all occupied states within the Brillouin zone (24, 33)

$$\sigma_{xy}^{\text{AHE}} = -\frac{2\pi e^2}{h} \sum_a \int \frac{d\mathbf{k}}{(2\pi)^3} f_a(\mathbf{k}) \Omega_a(\mathbf{k})$$

$$\Omega_a(\mathbf{k}) = \frac{2ih^2}{(2\pi)^2} \sum_{a \neq b} \frac{\langle \mathbf{k}, a | \hat{v}_x | \mathbf{k}, b \rangle \langle \mathbf{k}, b | \hat{v}_y | \mathbf{k}, a \rangle}{[E_a(\mathbf{k}) - E_b(\mathbf{k})]^2} \quad (1)$$

where e is the electron charge, h is the Planck's constant, and $f_a(\mathbf{k})$ denotes the Fermi-Dirac distribution of the occupied states. Regarding the Berry curvature $\Omega_a(\mathbf{k})$ in \mathbf{k} space, $\hat{v}_x = \frac{2\pi i}{h} [\hat{H}, \hat{r}_x]$ and $\hat{v}_y = \frac{2\pi i}{h} [\hat{H}, \hat{r}_y]$ represent the velocity operators along the x and y

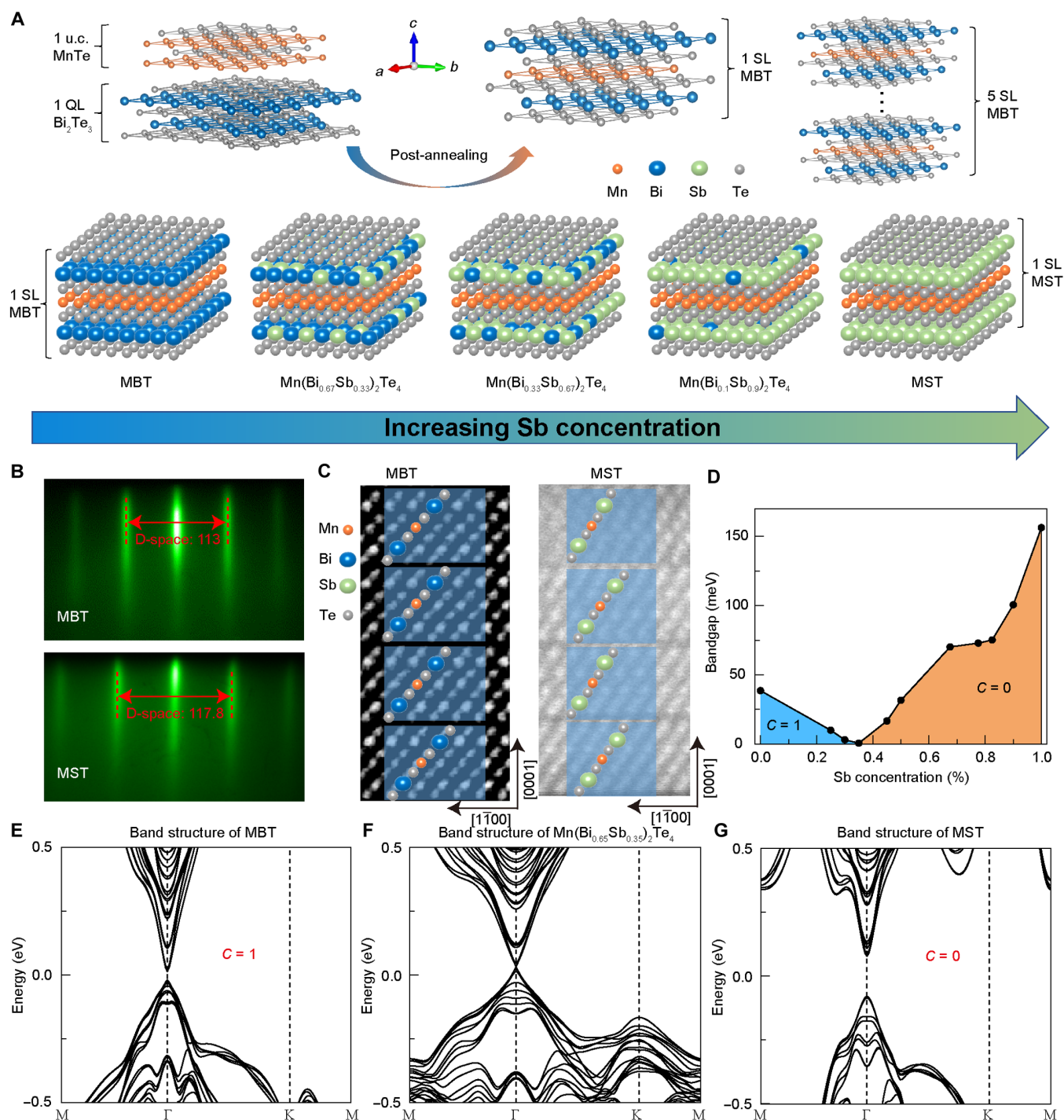


Fig. 1. Structural characterizations and DFT calculations of the MBE-grown $\text{Mn}(\text{Bi}_{1-x}\text{Sb}_x)_2\text{Te}_4$ thin films. (A) Schematic of the growth procedure of five SL MBST with varied Sb-to-Bi ratios, starting from a quintuple layer (QL) of Bi_2Te_3 and a unit cell (u.c.) of MnTe . (B) In situ RHEED patterns of the MBT and MST samples. The sharp streaky patterns sustain during the entire growth. The length of the double arrows changes from 113 (MBT) to 117.8 (MST) reciprocal lattice units, indicating a decrease in the in-plane lattice constant due to the incorporated Sb atoms. (C) Cross-sectional HR-STEM image of the MBT and MnSb_2Te_4 thin film grown on Al_2O_3 (0001) substrates. (D) Evolution of the energy gap with Sb content in the MBST system. The closing and reopening of the bandgap E_g at $x = 0.35$ imply that MBST experiences a topological phase transition from a Chern insulator ($C = 1$) to a normal insulator ($C = 0$). (E to G) Electronic band structures of the $x = 0, 0.35$, and 1 samples exemplify the topological phase transition in the MBST system.

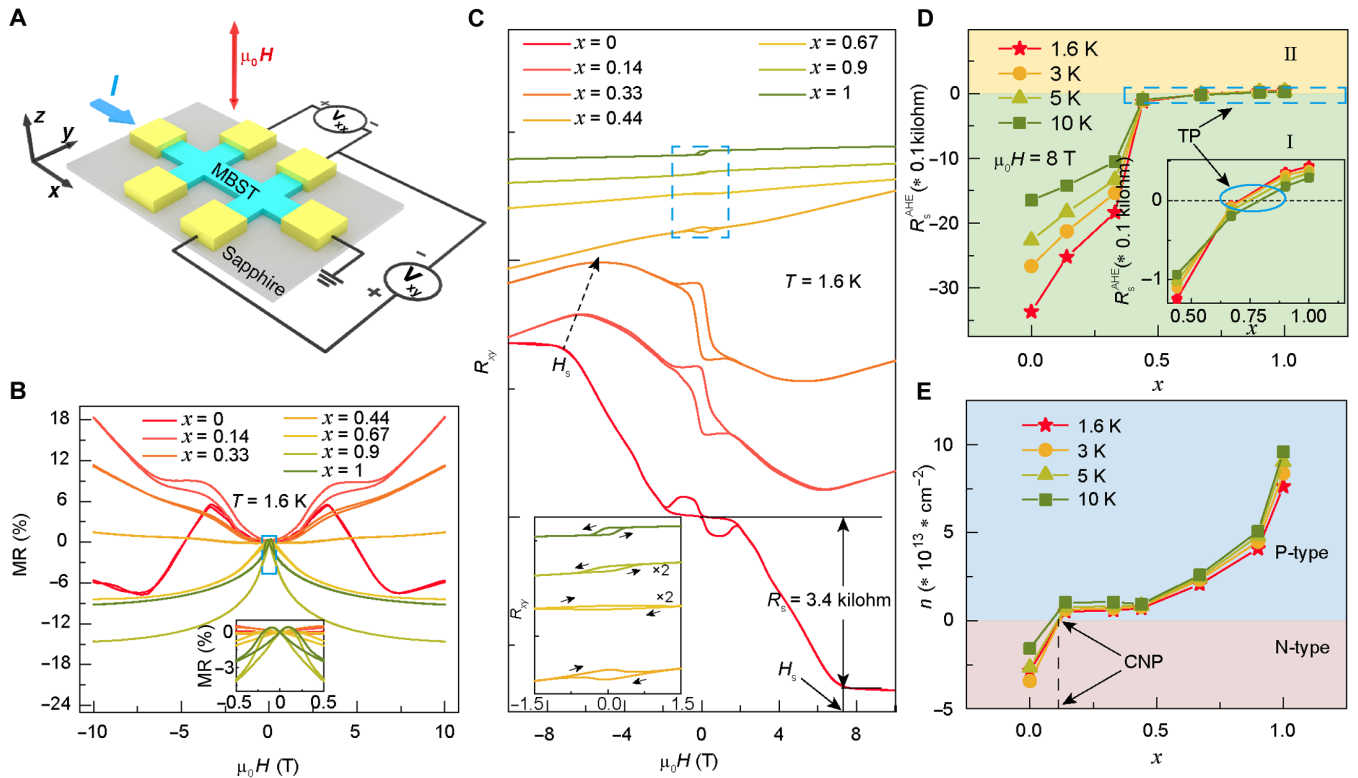


Fig. 2. MR and AHE in five SL $\text{Mn}(\text{Bi}_{1-x}\text{Sb}_x)_2\text{Te}_4$ thin films with $x = 0, 0.14, 0.33, 0.44, 0.67, 0.9$, and 1 . (A) Schematic of the six-terminal Hall bar device and the magneto-transport measurement setup. The input current I and magnetic field μ_0H are applied along the x and z axes, and the longitudinal (V_{xx}) and transverse (V_{xy}) voltages are recorded along the x and y directions, respectively. (B) Magnetic field-dependent MR data at $T = 1.6$ K. The overall MR curve gradually changes from the antiferromagnetic-type giant MR contour to the ferromagnet-like double-split butterfly line shape with the increase of the Sb content (inset). (C) Low-temperature anomalous Hall resistance of the MBST samples. With increasing Sb concentration, the saturation field H_s successively reduces and the AHE loop polarity changes when $x > 0.67$ (inset). The hybrid AHE observed in the MBT thin film may be caused by native antisite defects and/or random stacking order formed during sample growth. (D) Temperature-dependent saturated AHE resistance R_s^{AHE} ($\mu_0H = 8$ T) of the five SL MBST thin films, where the sign of R_s^{AHE} changes from negative to positive at $x \sim 0.67$ (inset) and the “TP” means transition point. (E) Carrier density as a function of Sb content x in the MBST samples. The charge neutral point (CNP) is located $x \sim 0.14$.

directions, while $\langle \mathbf{k}, a | \langle \mathbf{k}, b |$ and $E_a(\mathbf{k}) [E_b(\mathbf{k})$ denote the eigenvectors and eigenvalues of the Hamiltonian \hat{H} , respectively. Figure 3(B1 to B5) summarizes the calculated intrinsic σ_{xy}^{AHE} as a function of the chemical potential in the $\text{Mn}(\text{Bi}_{1-x}\text{Sb}_x)_2\text{Te}_4$ samples ($x = 0, 0.3, 0.67, 0.9$, and 1). It is seen that negative AHC pockets are well-developed for the $x = 0, 0.3$, and 0.67 cases, yet they progressively diminish as the Sb content increases. When $x > 0.67$, only positive AHC values are obtained in the $\sigma_{xy}^{\text{AHE}} - E$ spectra. These DFT simulation results suggest that the intrinsic σ_{xy}^{AHE} experiences a negative-to-positive transition as more Bi atoms are substituted by Sb, qualitatively consistent with our experimental data [i.e., to quantitatively reconstruct Fig. 3A, extrinsic contributions from side-jump and skew scatterings need to be considered in a more comprehensive AHC model for future studies (24)]. In alignment with such a critical AHC transition, the corresponding Berry curvature distributions of the two MBST samples ($x = 0.67$ and 0.9) within the k_x - k_y plane are provided in Fig. 3 (C and D). Comparing with the host MBT framework (fig. S3), we can see that while both MBST maps display a threefold symmetry-breaking feature, the amplitude of $\Omega_a(\mathbf{k})$ at each occupied (k_x, k_y) state exhibits a strong dependence on the Sb-to-Bi ratio, namely, the positive (negative) Berry curvature components dominate the $x = 0.67$ (0.9) sample, hence resulting in

an overall negative (positive) AHC [i.e., it is noted from Eq. 1 that the intrinsic σ_{xy}^{AHE} is negatively associated with the Berry curvature $\Omega_a(\mathbf{k})$ according to conventional definition (24)]. On this basis, the agreement between experimental and theoretical results confirms that the x -tailored Berry curvature can induce the sign reversal of the first-order anomalous Hall response in MBST thin films.

Tailoring second-harmonic polarity through chiral spin texture

In addition to the AHE, the second-harmonic magneto-transport signals of the MBST system were also investigated. Accordingly, the same set of five SL MBST samples ($0.33 \leq x \leq 1$) were fabricated into micrometer-size cross-bar devices, and Fig. 4A exemplifies the experimental setup of the angular-dependent second-harmonic measurement, in which the input current [$I = I_0 \sin(\omega t)$, $I_0 = 100$ μA , $\omega/2\pi = 31.3$ Hz] was applied along the x axis, and an external in-plane magnetic field of $|\mu_0H_{\text{in}}| = 8$ T was successively rotated within the xy plane (i.e., the angle between μ_0H_{in} and x axis is defined as φ). As illustrated in Fig. 4B, the effective spin-orbit field endowed by the intrinsic SOC can effectively convert the charge current into a nonequilibrium spin current whose scattering is affected by the magnetic moment of the MBST system (34). Under such circumstances, the nonreciprocal charge transport would arise where the

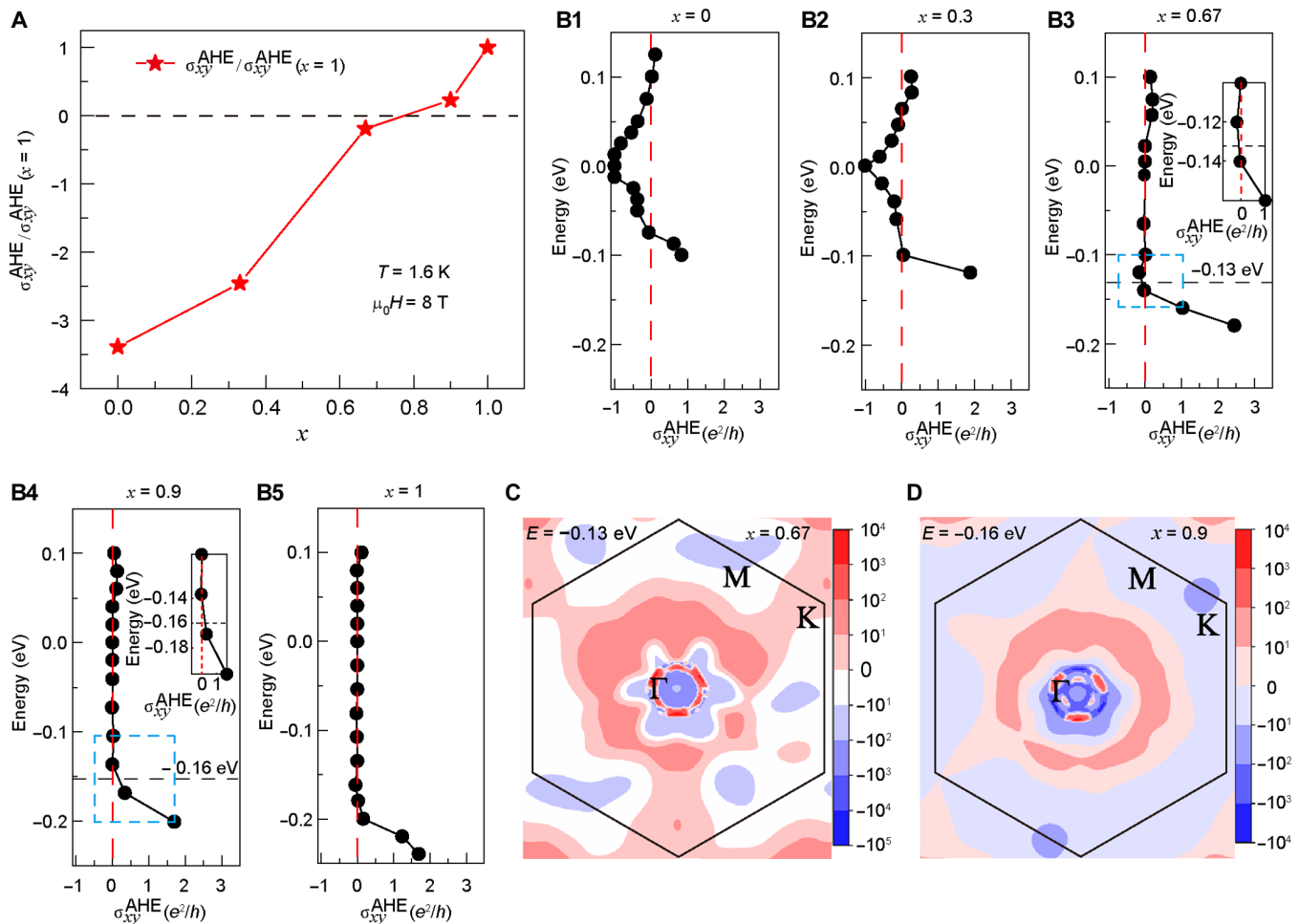


Fig. 3. Tailoring the AHC and Berry curvature via the Sb-to-Bi ratio engineering. (A) The normalized AHC displays a negative-to-positive transition in the five SL MBST samples at $T = 1.6$ K. (B1 to B5) The calculated intrinsic anomalous conductance as a function of the chemical potential. Negative AHC pockets are observed in the $x = 0, 0.3$, and 0.67 cases, whereas only positive AHC values are present in the $x = 0.9$ and 1 samples. The inset figures of (B3) and (B4) display the zoomed-in regions indicated by the light blue dashed boxes. (C and D) Berry curvature distributions at -0.13 eV (C) and -0.16 eV (D) corresponding to negative [inset of (B3)] and positive [inset of (B4)] AHC values, which visualize the competition between opposite Berry curvature components in the five SL MBST samples ($x = 0.67$ and 0.9). The integral of the Berry curvature in the k_x - k_y plane determines the intrinsic AHC polarity.

second-harmonic magneto-transport signals are odd with onefold symmetry under the reversal of either the charge current or the magnetic field (26). In agreement with the theoretical expectation (35–37), an unidirectional second-harmonic anomalous Hall resistance was observed in our five SL-MBST samples ($0.33 \leq x \leq 1$), where the measured second-harmonic Hall resistances $R_{xy}^{2\omega}(\varphi)$ curves all exhibit the sinusoidal dependence in reference to the rotation angle φ with the same period of 360° at $T = 1.6$ K, yet their relevant peak positions shift from $\varphi = 180^\circ$ ($x = 0.33, 0.44, 0.67, 0.9$, and 0.95) to $\varphi = 0^\circ$ ($x = 1$), as shown in Fig. 4C. Concurrently, the high-field amplitudes $\Delta R_{xy}^{2\omega} = [R_{xy}^{2\omega}(0^\circ) - R_{xy}^{2\omega}(180^\circ)]/2$ of the five SL MBST samples are found to maintain as negative or positive values regardless of the temperature variation (Fig. 4D). Such a different angular-dependent second-harmonic Hall response is also manifested in Fig. 4E, where the in-plane magnetic field-dependent $R_{xy}^{2\omega}$ curves of the $\text{Mn}(\text{Bi}_{0.05}\text{Sb}_{0.95})_2\text{Te}_4$ and MST thin films show opposite polarities under the same parallel and antiparallel ($\varphi = 0^\circ$ and

180°) $\mu_0 H_{\text{in}}-I$ configurations. This unique feature can be observed in the low-temperature region (e.g., $1.6 \text{ K} \leq T \leq 10 \text{ K}$), as shown in Fig. 4F.

Given that the polarity of the second-harmonic signal ($R_{xy}^{2\omega}$) is closely correlated with the spin texture of the magnetic MBST thin film (i.e., which determines the polarization of the spin current within the conduction channel) (38, 39), the observed peak/valley transition between the $x = 0.95$ and 1 samples indicates the reversal of the spin chirality direction. To understand the difference between the p -type $x = 0.95$ and $x = 1$ samples, their valence band (E_V) structures and the spin textures projected onto the k_x - k_y plane were subsequently calculated by first-principles calculations. As shown in Fig. 4 (G and H), the presence of SOC gives rise to the band splitting in the MBST system, and the resulting two sub-bands contain opposite spin chirality. It is identified that the spin direction of the outer sub-band for the $x = 0.95$ sample (counterclockwise blue arrows) is opposite to that of the $x = 1$ one (clockwise red arrows). Consequently, the overall dominant counterclockwise (clockwise)

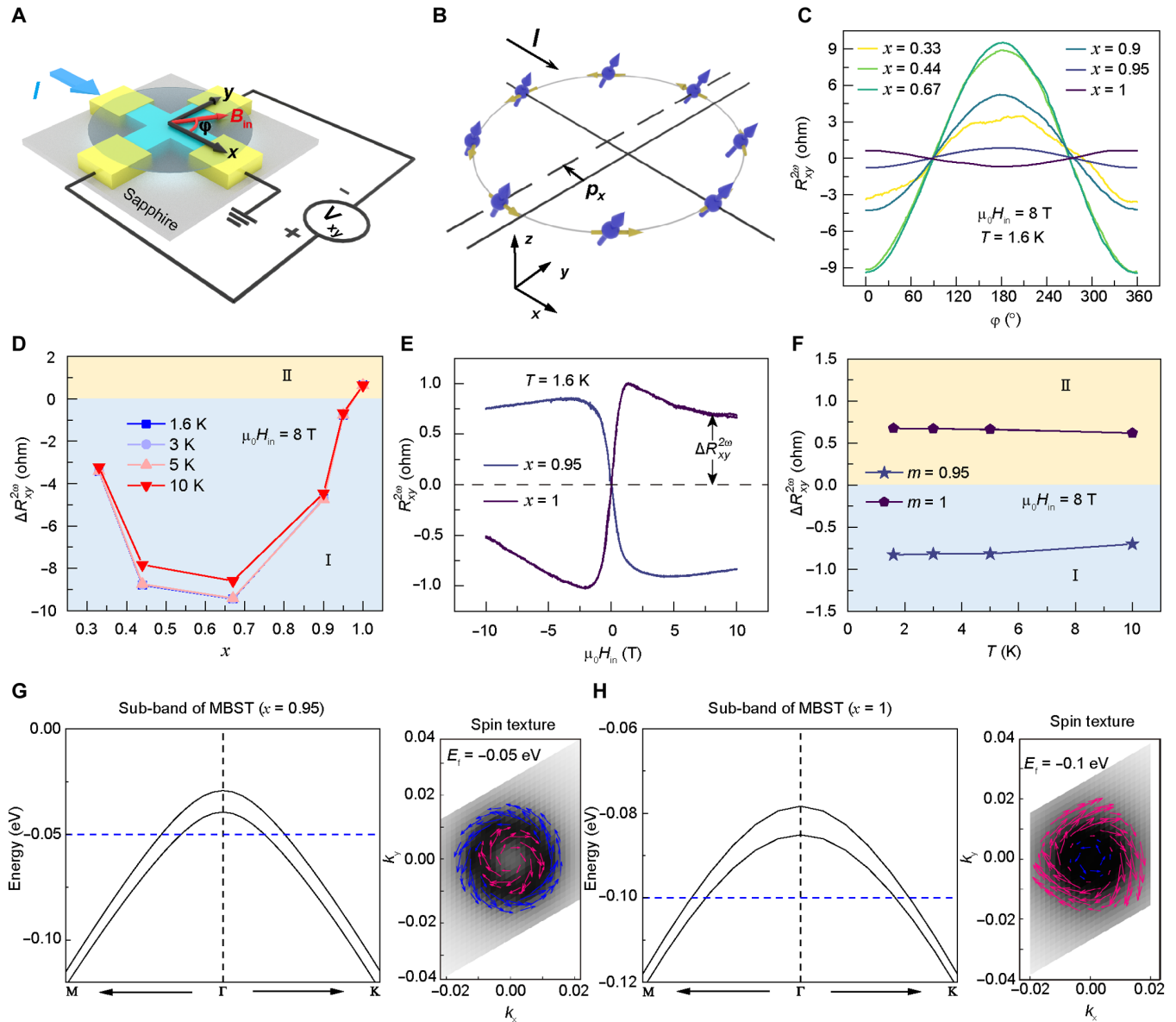


Fig. 4. Phase modulation of the unidirectional second-harmonic anomalous Hall resistance in the five SL MBST thin films. (A) Schematic of the cross-bar device structure and the angular-dependent second-harmonic measurement setup. The rotation angle is defined as the angle between the applied I and in-plane magnetic field $\mu_0 H_{in}$. (B) Illustration of the nonequilibrium spin accumulations generated along the k_x direction by the applied current. (C) Angular-dependent plots of $R_{xy}^{2\omega}$ for the MBST samples ($x = 0.33, 0.44, 0.67, 0.9, 0.95$, and 1) at $T = 1.6$ K and $|\mu_0 H_{in}| = 8$ T. All sinusoidal $R_{xy}^{2\omega}(\varphi)$ curves have the same period of 360° , yet a peak-to-valley transition occurs in the MST sample ($x = 1$). (D) Temperature-dependent $\Delta R_{xy}^{2\omega} = [R_{xy}^{2\omega}(0^\circ) - R_{xy}^{2\omega}(180^\circ)]/2$ extracted from the measured second-harmonic transport data, which confirms that the reversal of the $R_{xy}^{2\omega}(\varphi)$ curve is not caused by the temperature variation. (E) Magnetic field-dependent second harmonic signals of the $\text{Mn}(\text{Bi}_{0.05}\text{Sb}_{0.95})_2\text{Te}_4$ and MST samples at $T = 1.6$ K. Both current and in-plane magnetic field are applied along the x axis. (F) $\Delta R_{xy}^{2\omega} - T$ data from 1.6 to 10 K. (G and H) DFT-simulated valence band structures and corresponding spin texture mapping of the $x = 0.95$ MBST (G) and $x = 1$ MST (H) samples.

spin texture (i.e., which is the integration of the in-plane spin components from E_V to E_F) results in the accumulation of a nonequilibrium spin polarization along the $-y$ ($+y$)-direction of the five SL- $\text{Mn}(\text{Bi}_{0.05}\text{Sb}_{0.95})_2\text{Te}_4$ (MST) sample, which in turn is responsible for the appearance of the $\varphi = 180^\circ$ ($\varphi = 0^\circ$) peak position of the $R_{xy}^{2\omega}(\varphi)$ curve as well as the negative (positive) $R_{xy}^{2\omega}(0^\circ)$ at $|\mu_0 H_{in}| = 8$ T. In addition, our simulation results also reveal that the breaking of the periodic lattice condition along the z direction can introduce a

surface potential at the top MBST surface, and the corresponding potential gradients (∇V) are found to be opposite in $x = 0.95$ and 1 cases (fig. S4). Considering that the effective spin-orbit field direction is given by $\mathbf{B}_{SO} \propto \boldsymbol{\sigma} \cdot (\mathbf{p} \times \nabla V)$ (i.e., where $\boldsymbol{\sigma}$ and \mathbf{p} represent the Pauli spin matrix vector and the momentum operator, respectively), the spin states of the top surface states are thereafter polarized toward the $-y$ -axis ($\text{Mn}(\text{Bi}_{0.05}\text{Sb}_{0.95})_2\text{Te}_4$) and $+y$ -axis (MST). In other words, both the opposite spin chirality and potential gradient directions

support the possible physical origins of the second-harmonic $R_{xy}^{2\omega}$ polarity found in our measurement datasets.

DISCUSSION

In conclusion, we have demonstrated the precise control over the electronic band structure of MBST through systematic adjustment of the Sb-to-Bi ratio. This manipulation enables the tuning of the Berry curvature and spin texture at the Fermi level, which tailors both first- and second-harmonic magneto-transport responses in terms of MR line shape and polarity. The intrinsic interplay between SOC and spin/magnetic orders allows for spin polarization switching via effective band engineering, which may facilitate the further design of SOT-based devices with customizable chirality. With further explorations of the topological features embedded in the host MBT family matrix [e.g., MBST, MBT(Bi₂Te₃)_m, and MBST((Bi_{1-x}Sb_x)₂Te₃)_n], our results open up an avenue for the pursuit of energy-efficient topological spintronic applications.

METHODS

Sample growth and characterizations

Following our previous optimized growth recipe (30), the MBST samples ($x = 0, 0.14, 0.33, 0.44, 0.67, 0.9, 0.95$, and 1) were grown on Al₂O₃ (0001) substrates by MBE at a pressure of 1×10^{-8} Pa. The Al₂O₃ substrate was pre-annealed at 570°C before the sample growth. Next, high-purity Mn (99.9998%), Bi (99.99999%), Sb (99.99999%), and Te (99.99999%) atoms were coevaporated from standard Knudsen cells and cracker cells, and the ratio between the different elements (e.g., Bi and Sb) was validated using a beam flux monitor. Before obtaining the first MBST SL, monolayers of (Bi_{1-x}Sb_x)₂Te₃ and MnTe need to be deposited sequentially at 200° and 370°C, respectively, followed by a moderate post-annealing at 390°C. Meanwhile, the growth process was monitored by in situ RHEED. In addition, x-ray diffraction and x-ray photoelectron spectroscopy were performed to examine the crystal structure as well as to calibrate the ratio of Bi and Sb of the grown samples.

Device fabrication

The devices investigated in this work were obtained by a standard nanofabrication process. The MBE-grown five SL MBST thin films were firstly capped with a 1.4-μm-thick layer of photoresist before being exposed using a maskless photolithography system (MLA150). The micrometer-sized, six-terminal Hall bar and cross-bar patterns were defined by ion beam etching. Last, 160-nm-thick Ti/Au electrodes were deposited using an e-beam evaporator. All the processes were carried out in a cleanroom with International Organization for Standardization 5 (ISO-5) and ISO-6 level conditions.

Transport measurement

The magneto-transport measurements of the MBST-based devices were performed using a He⁴ refrigerator (Oxford Teslatron PT system), which provides a base temperature of as low as 1.5 K and the magnetic field up to ±14 T. Subsequently, standard lock-in measurements were performed, where the current amplitude was fixed at 1 μA (first-harmonic Hall measurements) and 100 μA (second-harmonic Hall measurements), respectively, and the lock-in frequency was modulated from 1 to 1000 Hz. As illustrated in Fig. 2A, the current conduction direction was defined as the x axis, following

the standard convention for six-terminal Hall bar devices, and the longitudinal (V_{xx}) and transverse (V_{xy}) voltages are recorded along the x and y directions during the magneto-transport measurements, respectively. The x and y directions are independent of the crystal orientation (see section S5). Both the first- and second-harmonic voltage signals were recorded simultaneously by SR-830 lock-in amplifiers (see section S6).

First-principles calculations

We used the projected augmented wave method as implemented in the VASP package (40) and generalized gradient approximation exchange-correlation potential in the calculations (41). A 2×2 supercell was built to simulate the properties of MBST with different Sb doping concentrations, and the $3d$ states of Mn were treated with the GGA + U approach with $U = 5.0$ eV (42). Meanwhile, the kinetic cutoff energy of the plane wave was set up to 350 eV. Subsequently, the Brillouin zone was sampled with a Γ -centered $4 \times 4 \times 1$ grid based on the scheme proposed by Monkhorst and Pack (43), a vacuum buffer space over 18 Å was included to prevent interaction between adjacent slabs, and the convergence criterion was set to 10^{-5} eV for energy in optimization and self-consistent calculations, respectively. Besides, the Hellmann-Feynman force tolerance criterion for convergence was 0.01 eV/Å, and the DFT-D3 method was adopted to describe the van der Waals force of the layered MBST (44). The maximally localized Wannier functions were constructed to calculate the topological-related properties and spin texture (45, 46).

Supplementary Materials

This PDF file includes:

Supplementary Text
Figs. S1 to S5
Table S1
References

REFERENCES AND NOTES

1. J. Sinova, S. O. Valenzuela, J. Wunderlich, C. Back, T. Jungwirth, Spin Hall effects. *Rev. Mod. Phys.* **87**, 1213 (2015).
2. M. I. Dyakonov, V. I. Perel, Current-induced spin orientation of electrons in semiconductors. *Phys. Lett. A* **35**, 459–460 (1971).
3. J. Sinova, D. Culcer, Q. Niu, N. Sinitsyn, T. Jungwirth, A. H. MacDonald, Universal intrinsic spin Hall effect. *Phys. Rev. Lett.* **92**, 126603 (2004).
4. S. Murakami, N. Nagaosa, S.-C. Zhang, Dissipationless quantum spin current at room temperature. *Science* **301**, 1348–1351 (2003).
5. A. Manchon, H. C. Koo, J. Nitta, S. M. Frolov, R. A. Duine, New perspectives for Rashba spin–Orbit coupling. *Nat. Mater.* **14**, 871–882 (2015).
6. V. M. Edelstein, Spin polarization of conduction electrons induced by electric current in two-dimensional asymmetric electron systems. *Solid State Commun.* **73**, 233–235 (1990).
7. M. Cubukcu, O. Boule, N. Mikuszeit, C. Hamelin, T. Brächer, N. Lamard, M.-C. Cyrille, L. Buda-Prejbeanu, K. Garello, I. M. Miron, O. Klein, G. de Loubens, V. V. Naletov, J. Langer, B. Ocker, P. Gambardella, G. Gaudin, Ultra-fast perpendicular spin–orbit torque MRAM. *IEEE Trans. Magn.* **54**, 1–4 (2018).
8. S. Parkin, S.-H. Yang, Memory on the racetrack. *Nat. Nanotechnol.* **10**, 195–198 (2015).
9. Z. Luo, A. Hrabec, T. P. Dao, G. Sala, S. Finizio, J. Feng, S. Mayr, J. Raabe, P. Gambardella, L. J. Heyderman, Current-driven magnetic domain-wall logic. *Nature* **579**, 214–218 (2020).
10. X. Wang, C. Wan, W. Kong, X. Zhang, Y. Xing, C. Fang, B. Tao, W. Yang, L. Huang, H. Wu, M. Irfan, X. Han, Field-free programmable spin logics via chirality-reversible spin–Orbit torque switching. *Adv. Mater.* **30**, 1801318 (2018).
11. S. Fukami, C. Zhang, S. DuttaGupta, A. Kurenkov, H. Ohno, Magnetization switching by spin–Orbit torque in an antiferromagnet–ferromagnet bilayer system. *Nat. Mater.* **15**, 535–541 (2016).
12. A. Kurenkov, S. DuttaGupta, C. Zhang, S. Fukami, Y. Horio, H. Ohno, Artificial neuron and synapse realized in an antiferromagnet/ferromagnet heterostructure using dynamics of spin–orbit torque switching. *Adv. Mater.* **31**, e1900636 (2019).

13. K. Garello, I. M. Miron, C. O. Avci, F. Freimuth, Y. Mokrousov, S. Blügel, S. Auffret, O. Boulle, G. Gaudin, P. Gambardella, Symmetry and magnitude of spin–orbit torques in ferromagnetic heterostructures. *Nat. Nanotechnol.* **8**, 587–593 (2013).
14. C.-F. Pai, L. Liu, Y. Li, H. Tseng, D. Ralph, R. Buhrman, Spin transfer torque devices utilizing the giant spin Hall effect of tungsten. *Appl. Phys. Lett.* **101**, 122404 (2012).
15. L. Liu, C.-F. Pai, Y. Li, H. W. Tseng, D. C. Ralph, R. A. Buhrman, Spin-torque switching with the giant spin Hall effect of tantalum. *Science* **336**, 555–558 (2012).
16. R. Ramaswamy, X. Qiu, T. Dutta, S. D. Pollard, H. Yang, Hf thickness dependence of spin–orbit torques in Hf/CoFeB/MgO heterostructures. *Appl. Phys. Lett.* **108**, 202406 (2016).
17. Q. L. He, T. L. Hughes, N. P. Armitage, Y. Tokura, K. L. Wang, Topological spintronics and magnetoelectronics. *Nat. Mater.* **21**, 15–23 (2022).
18. Y. Tokura, K. Yasuda, A. Tsukazaki, Magnetic topological insulators. *Nat. Rev. Phys.* **1**, 126–143 (2019).
19. Y. Fan, P. Upadhyaya, X. Kou, M. Lang, S. Takei, Z. Wang, J. Tang, L. He, L.-T. Chang, M. Montazeri, G. Yu, W. Jiang, T. Nie, R. N. Schwartz, Y. Tserkovnyak, K. L. Wang, Magnetization switching through giant spin–orbit torque in a magnetically doped topological insulator heterostructure. *Nat. Mater.* **13**, 699–704 (2014).
20. Y. Fan, X. Kou, P. Upadhyaya, Q. Shao, L. Pan, M. Lang, X. Che, J. Tang, M. Montazeri, K. Murata, L. T. Chang, M. Akyol, G. Yu, T. Nie, K. L. Wong, J. Liu, Y. Wang, Y. Tserkovnyak, K. L. Wang, Electric-field control of spin–Orbit torque in a magnetically doped topological insulator. *Nat. Nanotechnol.* **11**, 352–359 (2016).
21. K. Yasuda, A. Tsukazaki, R. Yoshimi, K. Kondou, K. Takahashi, Y. Otani, M. Kawasaki, Y. Tokura, Current-nonlinear Hall effect and spin–orbit torque magnetization switching in a magnetic topological insulator. *Phys. Rev. Lett.* **119**, 137204 (2017).
22. J. Han, A. Richardella, S. A. Siddiqui, J. Finley, N. Samarth, L. Liu, Room-temperature spin–orbit torque switching induced by a topological insulator. *Phys. Rev. Lett.* **119**, 077702 (2017).
23. L. Tian, Y. Liu, W. Meng, X. Zhang, X. Dai, G. Liu, Spin–orbit coupling-determined topological phase: Topological insulator and quadratic Dirac semimetals. *J. Phys. Chem. Lett.* **11**, 10340–10347 (2020).
24. N. Nagaosa, J. Sinova, S. Onoda, A. H. MacDonald, N. P. Ong, Anomalous hall effect. *Rev. Mod. Phys.* **82**, 1539–1592 (2010).
25. Z. Zhang, N. Wang, N. Cao, A. Wang, X. Zhou, K. Watanabe, T. Taniguchi, B. Yan, W.-B. Gao, Controlled large non-reciprocal charge transport in an intrinsic magnetic topological insulator MnBi₂Te₄. *Nat. Commun.* **13**, 6191 (2022).
26. K. Yasuda, T. Morimoto, R. Yoshimi, M. Mogi, A. Tsukazaki, M. Kawamura, K. S. Takahashi, M. Kawasaki, N. Nagaosa, Y. Tokura, Large non-reciprocal charge transport mediated by quantum anomalous Hall edge states. *Nat. Nanotechnol.* **15**, 831–835 (2020).
27. M. M. Otrokov, T. V. Menshchikova, M. G. Vergniory, I. P. Rusinov, A. Y. Vyazovskaya, Y. M. Koroteev, G. Bihlmayer, A. Ernst, P. M. Echenique, A. Arnau, Highly-ordered wide bandgap materials for quantized anomalous Hall and magnetoelectric effects. *2D Mater.* **4**, 025082 (2017).
28. B. Chen, F. Fei, D. Zhang, B. Zhang, W. Liu, S. Zhang, P. Wang, B. Wei, Y. Zhang, Z. Zuo, J. Guo, Q. Liu, Z. Wang, X. Wu, J. Zong, X. Xie, W. Chen, Z. Sun, S. Wang, Y. Zhang, M. Zhang, X. Wang, F. Song, H. Zhang, D. Shen, B. Wang, Intrinsic magnetic topological insulator phases in the Sb doped MnBi₂Te₄ bulks and thin flakes. *Nat. Commun.* **10**, 4469 (2019).
29. S. H. Lee, D. Graf, L. Min, Y. Zhu, H. Yi, S. Ciocys, Y. Wang, E. S. Choi, R. Basnet, A. Fereidouni, A. Wegner, Y. F. Zhao, K. Verlinde, J. He, R. Redwing, V. Gopalan, H. O. H. Churchill, A. Lanzara, N. Samarth, C. Z. Chang, J. Hu, Z. Q. Mao, Evidence for a magnetic-field-induced ideal type-II Weyl state in antiferromagnetic topological insulator Mn(Bi_{1-x}Sb_x)₂Te₄. *Phys. Rev. X* **11**, 031032 (2021).
30. P. Chen, Q. Yao, J. Xu, Q. Sun, A. J. Grutter, P. Quarterman, P. P. Balakrishnan, C. J. Kinane, A. J. Caruana, S. Langridge, Tailoring the magnetic exchange interaction in MnBi₂Te₄ superlattices via the intercalation of ferromagnetic layers. *Nat. Electron.* **6**, 18–27 (2023).
31. J.-Q. Yan, S. Okamoto, M. A. McGuire, A. F. May, R. J. McQueeney, B. C. Sales, Evolution of structural, magnetic, and transport properties in MnBi_{2-x}Sb_xTe₄. *Phys. Rev. B* **100**, 104409 (2019).
32. R. Watanabe, R. Yoshimi, M. Kawamura, Y. Kaneko, K. S. Takahashi, A. Tsukazaki, M. Kawasaki, Y. Tokura, Enhancement of anomalous Hall effect in epitaxial thin films of intrinsic magnetic topological insulator MnBi₂Te₄ with Fermi-level tuning. *Appl. Phys. Lett.* **120**, 031901 (2022).
33. D. Xiao, M.-C. Chang, Q. Niu, Berry phase effects on electronic properties. *Rev. Mod. Phys.* **82**, 1959 (2010).
34. X. Chen, S. Shi, G. Shi, X. Fan, C. Song, X. Zhou, H. Bai, L. Liao, Y. Zhou, H. Zhang, A. Li, Y. Chen, X. Han, S. Jiang, Z. Zhu, H. Wu, X. Wang, D. Xue, H. Yang, F. Pan, Observation of the antiferromagnetic spin Hall effect. *Nat. Mater.* **20**, 800–804 (2021).
35. C. O. Avci, K. Garello, A. Ghosh, M. Gabureac, S. F. Alvarado, P. Gambardella, Unidirectional spin Hall magnetoresistance in ferromagnet/normal metal bilayers. *Nat. Phys.* **11**, 570–575 (2015).
36. G. Liu, X. Wang, Z. Luan, L. Zhou, S. Xia, B. Yang, Y. Tian, G.-h. Guo, J. Du, D. Wu, Magnonic unidirectional spin Hall magnetoresistance in a heavy-metal–ferromagnetic-insulator bilayer. *Phys. Rev. Lett.* **127**, 207206 (2021).
37. Y. Lv, J. Kally, D. Zhang, J. S. Lee, M. Jamali, N. Samarth, J.-P. Wang, Unidirectional spin-Hall and Rashba–Edelstein magnetoresistance in topological insulator-ferromagnet layer heterostructures. *Nat. Commun.* **9**, 111 (2018).
38. S.-H. C. Baek, V. P. Amin, Y.-W. Oh, G. Go, S.-J. Lee, G.-H. Lee, K.-J. Kim, M. D. Stiles, B.-G. Park, K.-J. Lee, Spin currents and spin–orbit torques in ferromagnetic trilayers. *Nat. Mater.* **17**, 509–513 (2018).
39. H. Masuda, T. Seki, J.-I. Ohe, Y. Nii, H. Masuda, K. Takanashi, Y. Onose, Room temperature chirality switching and detection in a helimagnetic MnAu₂ thin film. *Nat. Commun.* **15**, 1999 (2024).
40. G. Kresse, J. Furthmüller, Efficient iterative schemes for ab initio total-energy calculations using a plane-wave basis set. *Phys. Rev. B Condens. Matter* **54**, 11169–11186 (1996).
41. J. P. Perdew, K. Burke, M. Ernzerhof, Generalized gradient approximation made simple. *Phys. Rev. Lett.* **77**, 3865–3868 (1996).
42. V. I. Anisimov, J. Zaanen, O. K. Andersen, Band theory and Mott insulators: Hubbard U instead of Stoner I. *Phys. Rev. B Condens. Matter* **44**, 943–954 (1991).
43. H. J. Monkhorst, J. D. Pack, Special points for Brillouin-zone integrations. *Phys. Rev. B* **13**, 5188 (1976).
44. S. Grimme, J. Antony, S. Ehrlich, H. Krieg, A consistent and accurate ab initio parametrization of density functional dispersion correction (DFT-D) for the 94 elements H–Pu. *J. Chem. Phys.* **132**, 154104 (2010).
45. A. A. Mostofi, J. R. Yates, Y.-S. Lee, I. Souza, D. Vanderbilt, N. Marzari, wannier90: A tool for obtaining maximally-localised Wannier functions. *Comput. Phys. Commun.* **178**, 685–699 (2008).
46. Q. Wu, S. Zhang, H.-F. Song, M. Troyer, A. A. Soluyanov, WannierTools: An open-source software package for novel topological materials. *Comput. Phys. Commun.* **224**, 405–416 (2018).
47. H. Li, S. Liu, C. Liu, J. Zhang, Y. Xu, R. Yu, Y. Wu, Y. Zhang, S. Fan, Antiferromagnetic topological insulator MnBi₂Te₄: Synthesis and magnetic properties. *Phys. Chem. Chem. Phys.* **22**, 556–563 (2020).
48. H. Li, Y. Li, Y. Lian, W. Xie, L. Chen, J. Zhang, Y. Wu, S. Fan, Glassy magnetic ground state in layered compound MnSb₂Te₄. *Sci. China Mater.* **65**, 477–485 (2022).
49. Y. Deng, Y. Yu, M. Z. Shi, Z. Guo, Z. Xu, J. Wang, X. H. Chen, Y. Zhang, Quantum anomalous Hall effect in intrinsic magnetic topological insulator MnBi₂Te₄. *Science* **367**, 895–900 (2020).
50. C. Liu, Y. Wang, H. Li, Y. Wu, Y. Li, J. Li, K. He, Y. Xu, J. Zhang, Y. Wang, Robust axion insulator and Chern insulator phases in a two-dimensional antiferromagnetic topological insulator. *Nat. Mater.* **19**, 522–527 (2020).
51. X. Kou, Y. Fan, K. L. Wang, Review of quantum Hall trio. *J. Phys. Chem. Solid* **128**, 2–23 (2019).
52. C. Song, R. Zhang, L. Liao, Y. Zhou, X. Zhou, R. Chen, Y. You, X. Chen, F. Pan, Spin–orbit torques: Materials, mechanisms, performances, and potential applications. *Prog. Mater. Sci.* **118**, 100761 (2021).

Acknowledgments

Funding: This work is sponsored by the National Key R&D Program of China (grant no. 2023YFB4404000 to X.K.), National Natural Science Foundation of China (grant nos. 92164104 to X.K., 11974327 and 12474158 to Z.Q.), the Major Project of Shanghai Municipal Science and Technology (grant no. 2018SHZDZX02 to X.K.), the Shanghai Engineering Research Center of Energy Efficient and Custom AI IC, the ShanghaiTech Material Device and Soft Matter Nano-fabrication Labs (SMN180827 to X.K.), and the China Postdoctoral Science Foundation (2023M733411 and 2023TQ0347 to Z. Li). X.K. acknowledges support from the Shanghai Rising-Star Program (grant no. 21QA1406000) and the Open Fund of State Key Laboratory of Infrared Physics. Z.Q. acknowledges support from the Innovation Program for Quantum Science and Technology (2021ZD0302800) and the Anhui Initiative in Quantum Information Technologies (grant no. AHY170000). The supercomputing service of USTC and AM-HPC is gratefully acknowledged. Z. Liu acknowledges the support from the National Nature Science Foundation of China (92365204 and 12274298) and the National Key R&D program of China (grant no. 2022YFA1604400/03). **Author contributions:** X.K. conceived the experiment, and X.K., Z.Q., and T.H. supervised the study. P.C., Y.Z., J.L., X.L., G.Y., and Z. Liu grew the samples, performed material characterizations, and conducted the transport measurements. Q.S., J.Z., A.L., and X.H. performed HR-TEM microscopy characterization. P.C., P.H., J.L., T.H., Q.Y., L.L., J.L., and Y.Y. analyzed magneto-transport data. P.C., P.H., and X.C. fabricated the device. Z. Li and Z.Q. contributed to the first-principles calculations including band structures, spin texture, and the distribution of Berry curvature. P.C., P.H., Z. Li, T.H., Z.Q., and X.K. wrote the manuscript. All authors discussed the results and commented on the manuscript. **Competing interests:** The authors declare that they have no competing interests. **Data and materials availability:** All data needed to evaluate the conclusions in the paper are present in the paper and/or the Supplementary Materials.

Submitted 3 October 2024

Accepted 14 April 2025

Published 16 May 2025

10.1126/sciadv.adt6084